

UDK 53.086;622.785

ZnTiO₃ Ceramic Nanopowder Microstructure Changes During Compaction

N. Labus¹, J. Krstić², S. Marković¹, D. Vasiljević-Radović²,
M V. Nikolić³, V. Pavlović¹

¹Institute of Technical Sciences of SASA, Knez Mihajlova 35/IV, 11000 Belgrade, Serbia

²Institute of Chemistry, Technology and Metallurgy, Department of Catalysis and Chemical Engineering, University of Belgrade, Njegoseva 12, 11000 Belgrade, Serbia; Labs: Faculty of Chemistry, Studentski trg 12-16, III floor, Room 606.

³Institute for Multidisciplinary Research, University of Belgrade, Kneza Višeslava 1a, 11000 Belgrade, Serbia

Abstract:

ZnTiO₃ nanopowder as a constitutive component in compact production was primarily characterised. Scanning electron micrographs of as received powder were recorded. Mercury porosimetry and nitrogen adsorption were also performed on loose powder. Particle size distribution in a water powder suspension was determined with a laser particle size analyser. Compaction was performed on different pressures in a range from 100 to 400 MPa using the uniaxial double sided compaction technique without binder and lubricant. Micrographs of compacted specimens were obtained using scanning electron microscopy and atomic force microscopy. Pore size distribution was also determined by mercury porosimetry and nitrogen adsorption. Results revealed that with increasing pressure during compaction interagglomerate pores diminish in size until they reach some critical diameter related to the intra-agglomerate pore size.

Keywords: Compaction, Nanopowder, Pore size distribution, Nitrogen adsorption, Mercury porosimetry

1. Introduction

The compaction process is mainly regarded as a pressure – density relation which is afterwards compared with an appropriate compacting equation in order to recognize characteristic pressure domain ranges [1,2]. Although this approach is usable and allows density prediction, it does not lead to the processes and mechanisms responsible for compact densification. The compact density gradient shows that the applied pressure distribution is not uniform [3,4]. If we neglect the green body shape and different compaction techniques and means, an unavoidable aspect is concerned with the pressure distribution through interparticle contacts. With smaller particles the number of contacts in a bulk compacted specimen is vastly enlarged [5]. In the lowest pressure range, a still elastic mechanical contact invokes pressure distribution through different domains of compact as an elastic strain response that

*) Corresponding author: nebojsa.labus@itn.sanu.ac.rs

transfers the applied stress through different domains [6]. When friction between particles is overwhelmed by the distributed applied pressure, a particle rearrangement process takes place [7]. With increased applied pressures, the compact undergoes the process of particle deformation [8,9]. If brittle ceramic materials are used, deformation consists of micro crack propagation and fracture [10], while for ductile metal powders dislocation creep at yield point occurs [11,12]. Applying larger pressures, order of tens GPa magnitude, phase transition rearrangements are present on the atomic scale and consequently expected demands for characterization techniques follow [13].

Powder particle size in the nanodimension range is of great interest due to specific phenomena. Namely nano powders show high agglomeration tendency and particles are arranged into specific assemblies and agglomerates [14]. A common phenomenon is that compacts within the same range of pressures have an attainable density lower than with compacting micro particles [15]. Also, compacted nano powders thus show a high degree of porosity, and increased shrinkage rate coupled with lowered sintering temperature [16].

This work is an attempt to explain changes of compacts made of ZnTiO₃ ceramic nano powder compacted without binder or lubricant at applied compaction pressures that are beyond the particles deformation mechanism pressure range. Also, applied characterization techniques are all conventional, and are concerned with particle and pore interactions as a function of compaction pressure. In the observed scale, changes indicate the specific behavior of structural organization of ceramic nanoparticles during green body formation.

2. Experimental

ZnTiO₃ nanopowder, Aldrich [CAS 112036-43-0] was used in the compaction process. Theoretical density from JCPDS ZnTiO₃ 26-1500 [17] is declared as 5.165 g/cm³. The density of a poured as received loose powder measured on the same amount of powder weight as a compact is termed ρ_0 , and equals 0.213 g/cm³. As received nanopowder was characterised on JEOL instruments model JSM-6610. Nitrogen adsorption-desorption isotherms of loose powder were collected on a Sorptomatic 1990 Thermo Finningen at 77 K. Prior to the adsorption, samples were outgassed for 18 hours at 383 K under a residual pressure less than 0.2 Pa and additional 2 hours at residual pressure lower than 2 μ Pa. ADP software Version 5.13 CE Instruments was used to analyze the resulting isotherms. Mercury porosimetry was conducted with as received powder and also on powder suspended in ethanol and afterwards evaporated by outgassing during 8 hours at pressure less than 500 Pa in a measuring piston on Porosimeter 2000 FISIONS instruments. Obtained mercury porosimetry data were processed with software package Pascal Ver.1.05. Two intrusion-extrusion runs, denoted as R1 and R2, were conducted on the same powder specimens. Optical particle size distribution for non compacted powder was done on Malvern Instruments Ltd., Master sizer 2000, Ver. 5.54., with a Hydro 2000 S(A) adapter in water as a dispersant, within the size range from 60 to 2000 nm, including previous treatment in an ultrasonic bath for 10 minutes.

Compaction was conducted on a hydraulic press RING, P-14, VEB Thuringer, in a tool 8 mm in diameter consisting of a die and cylinder, with double sided uniaxial compaction process. Compact shapes were cylindrical, with mass of approximately 0.5 g. No previous treatment was performed on the powder submitted to compaction neither was a binder used nor was the tool lubricated. Applied pressures were 100, 200, 300, 400 MPa, and were sustained for 1 minute. Compacts were characterised by microstructure analysis on breakage surfaces with a scanning electron microscope (SEM) model JEOL JSM 6390, while atomic force microscopy (AFM) was performed on a Thermo microscopes autoprobe CP Research device on the surface of compacts pressed under 200 MPa. Specific surface area by nitrogen adsorption and mercury porosimetry used the same equipment as mentioned before. Pore size distributions were calculated for compacted specimens.

Compact bulk densities were determined by two different means. Dimensions for bulk densities of compacts were determined by measurement of mass, height and diameter for presumed compacts ideal cylinder shape. Also bulk densities were obtained by mercury pycnometry on atmospheric pressure and room temperature. Apparent densities of compacts represent skeletal density of compacted specimen. It is obtained during mercury porosimetry measurements as non-intruded volume by mercury. Apparent density was also calculated as the difference between mercury pycnometry bulk density and amount of nitrogen uptake at maximal uptake volume at corresponding relative pressure, termed as Gurvitch volume.

3. Results and discussion

3.1. Nanopowder

Powders with fine particles are prone to agglomeration. Weakly bound powder particles are arranged in space on different size scales. We can define interagglomerate pores formed between nanopowder particles and intragglomerate pores as voids formed by attached neighbour agglomerates.

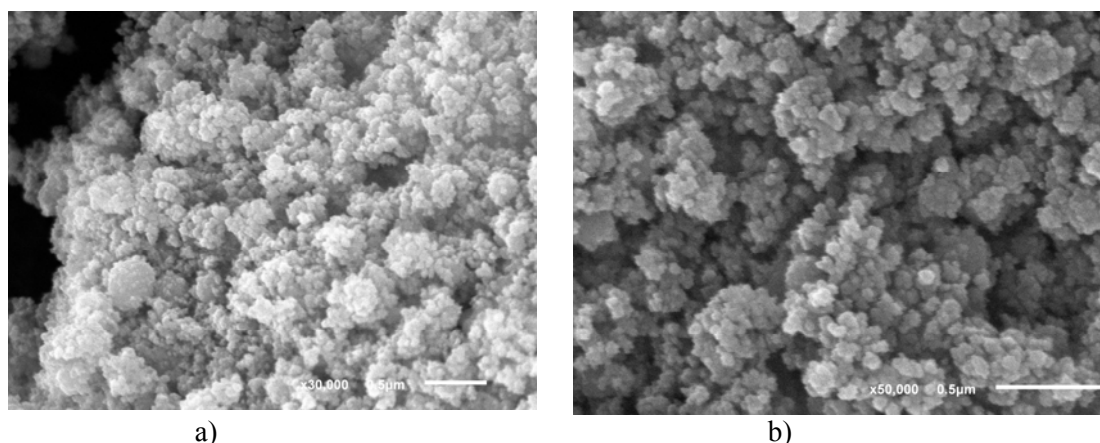


Fig. 1. Scanning electron micrographs of as received nanopowder in **a)** 30.000 times magnification and **b)** 50.000 times magnification.

Micrographs presented on fig.1. show different types of agglomerates formed from nanodimensional powder particles. Agglomerates are spherical but not uniform in shape, and mutually separated with irregular voids, fig.1.a). At the same time powder particles constituting agglomerates are hardly distinguishable on the larger magnification presented on fig.1.b).

On fig.2.a), nitrogen adsorption on a loose powder isotherm is resembling type II [18], characteristic for nonporous solids. From the specific surface area value of $41.7 \text{ m}^2/\text{g}$ obtained by the BET procedure, the estimated volume-surface mean diameter of a particle is 29 nm. Loose powder was submitted to mercury porosimetry measurements as non treated – as received (a.r.powder) and also as a powder obtained from an evaporated ethanol suspension (powder+EtOH). For both samples intrusion-extrusion curves (int-ext) are presented on fig.2.b). Two subsequent runs on the same sample are denoted as R1 and R2. According to fig. 2. we conclude that during the first run intrusion R1 two simultaneous processes occur. The first one is that the inter-agglomerate pore structure is diminishing in volume, along with the second one where interagglomerate pores are penetrated by liquid mercury. Intrusion curves thus resemble the one with the mechanism described as buckling of the filament [19]. Pores crush until pore sizes smaller than a certain critical pore size. Pores,

with a smaller size than the critical size, remain unchanged when afterwards, the mechanism changes to subsequent mercury intrusion of firmly packed powder particles. Here pore connectivity is undistinguishable and the overall powder particle coordination number is undefined [20]. A mechanism shift is at 30 MPa which resembles a pore diameter of 50 nm, again, leads to agglomerates 100 to 200 nm in size [21]. Subsequent runs are instructing that the system does not show elastic behaviour in the observed higher pressure range, but we can indicate that after 30 MPa mercury pressure penetration, although with slight differences, originates from the same mechanism for R1 and R2. Differences between ethanol treated and non-treated as received powder are significant when extrusion curves are compared. For as received powder all mercury in a two regarded subsequent runs R1 and R2 show clear retention of mercury, indicating that the structure most likely consisted of tubular forms with narrow constrictions, similar with the ink bottle type. Opposite to this, regarding ethanol treated powder, extrusion curves showed on fig.2.b), we note that for first run R1 and for second run R2, intruded mercury completely leaves the pore system.

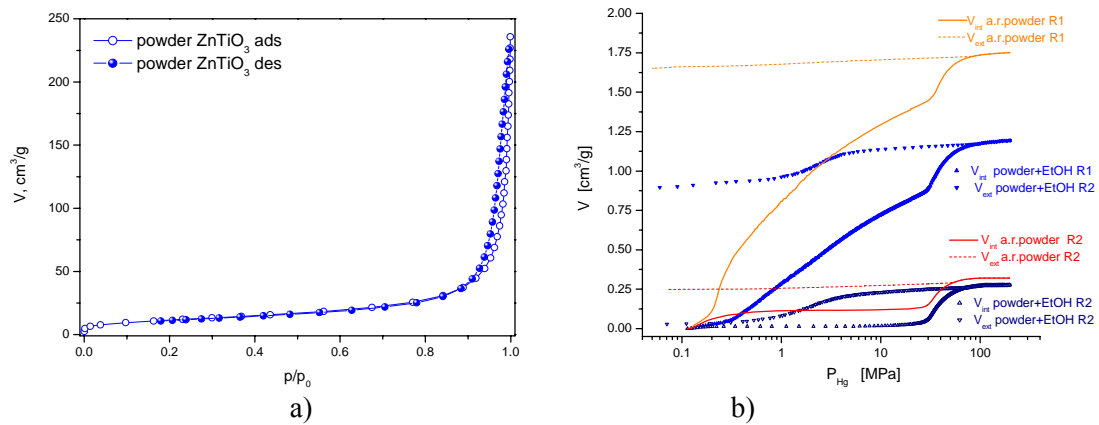


Fig. 2. a) Nitrogen adsorption-desorption isotherm for as received loose powder and b) mercury porosimetry intrusion-extrusion curves for loose powder treated with ethanol and as received with two subsequent runs R1 and R2.

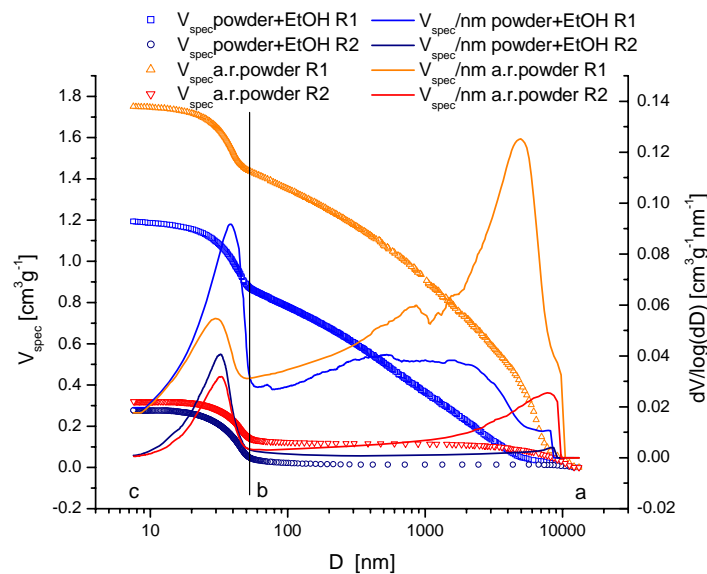


Fig. 3. Cumulative pore volume distribution and pore volume distribution as a function of pore size for loose powder treated with ethanol and as received including two subsequent runs R1 and R2.

Since mercury penetration is observing different mechanisms, according to pore volume distribution curves on fig.3, instructive comparison of intruded volumes is between the second, denoted as bc, and preceding first, ab, volume region, tab.1. We must notice that the pore crushing model on the as received loose powder shows an intensive peak in the interagglomerate volume, region ab, at pore sizes of 5 microns, which is lacking in the ethanol treated powder, where a broad peak from 0.3 to 2 microns pore diameter is observed. Intra-agglomerate pore structure, region bc, equal 50 nm pore size and less, seems from the pore volume distribution curve shape mostly unaffected by intrusion-extrusion repeating runs, R1 and R2. Thus, the same run intrusion volume calculations are indicative for first run R1 where the interagglomerate volume is estimated as 84% for a.r.powder and 74.5% for ethanol treated tab.I.

Tab. I Characteristic values of intruded volume in mercury porosimetry for loose powder.

a→c V_c [mm ³ g ⁻¹]	a→b V_b [mm ³ g ⁻¹]	c→b V_c-V_b [mm ³ g ⁻¹]	c→b % V_c-V_b [% V_c]	a→b% V_b [% V_c]	Powder treatment
Run 1 R1					
1750	1468	282	16.1	83.9	a.r.powder
1193	889	304	25.1	74.5	powder+EtOH
Run 2 R2					
320	140	180	56.2	43.8	a.r.powder
277	45	232	83.7	16.2	powder+EtOH

Since the two successive runs for differently treated specimens, fig.3, are performed on the same material, and in accordance with the previous discussion, we would also emphasize the difference between total intruded volumes for the first R1 and second run R2, which also represent the entire intraagglomerate volume. The estimated R1-R2 volume difference for the as received powder equals 1430 mm³/g, and for ethanol treated 916 mm³/g. Calculated in percentage it represents 82% of the total intruded volume occupied by inter-agglomerate volume voids for as received, and 76% for ethanol treated powder. This enables us to confirm the difference between the inter-agglomerate and intra-agglomerate pore system, tab.I, and also declare a firmly established structure of pore system composed from powder particles where the overall coordination number is extremely increased.

In a liquid suspended nanopowder, powder particle size distributions refer to the size and population numerosity of different agglomerate sizes. According to this, the particle size distribution is influenced by powder interactions with the observed liquid and by previous deagglomeration treatment. In the observed system, the powder particle size distribution presented in fig.4, is obtained as an ultrasonically treated water suspension of as received powder. According to the number percentage distribution, almost all particles are regarded as agglomerates up to 700 nm diameter. The volume percentage particle size distribution of agglomerates shows bimodal behaviour. Particles with smaller volumes are corresponding particle sizes of numerous agglomerates at 300 nm diameter peak, respectively. The second most populated volumetric percentage distribution agglomerates size peak is in the size of 2.5 microns. Distribution includes particles up to 4.5 microns. This characterisation is in agreement with obtained values before the mentioned Hg porosimetry powder characterisation.

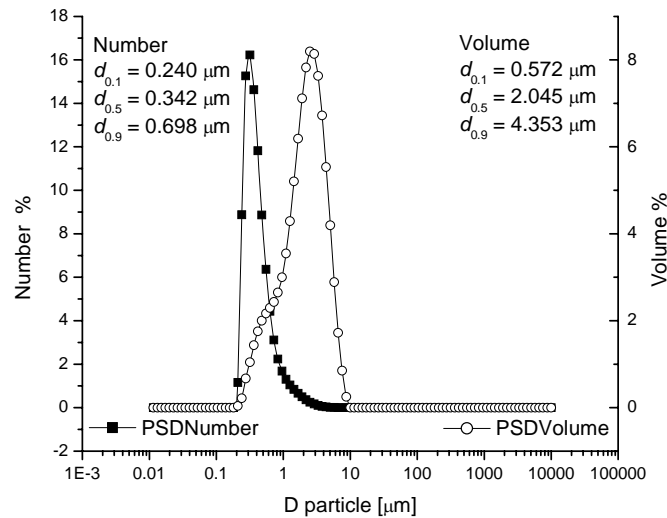


Fig 4. Powder particle size distribution presented as a fraction of number of particles attached to distinct particle diameter, and particle size distribution presented as percentage of all particles volume.

3.2. Compacted specimens

The observed pressure range from 100 to 400 MPa was determined since below 100 MPa adhesion on the tool cylinder significantly changes the compact shape and at the higher pressures than 400 MPa lamination through radial direction occurs. SEM and AFM micrographs in fig.5 and fig.6 show that compacted specimens display still visible powder particles spherical entities and grouped agglomerates. Compared with loose powder micrographs on fig.1, agglomerates in compacts are separated by large crack shape irregularities.

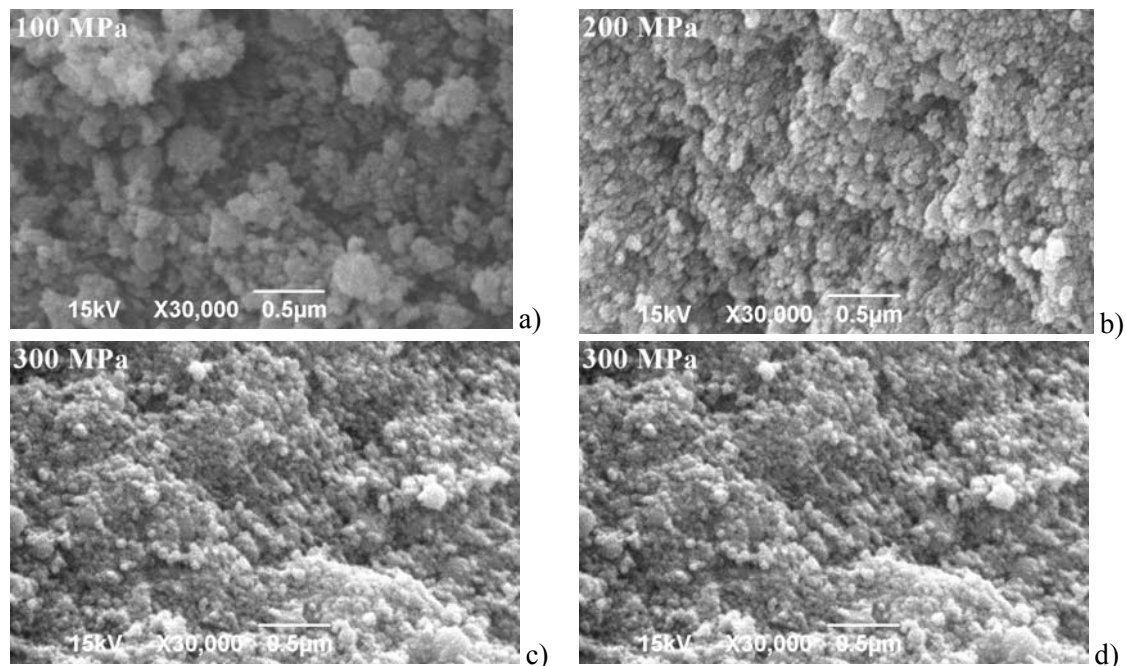


Fig. 5. Scanning electron micrographs of compacted specimens 100, 200, 300, 400 MPa.

On an AFM surface image of the compact treated at 200 MPa pressure, fig.6, we can distinguish cracks as a darker field spreading across the picture. According to the gradient bar, (left corner of fig.6.) these laminar cracks are varying in depth from 150 to 300 nm, respectively.

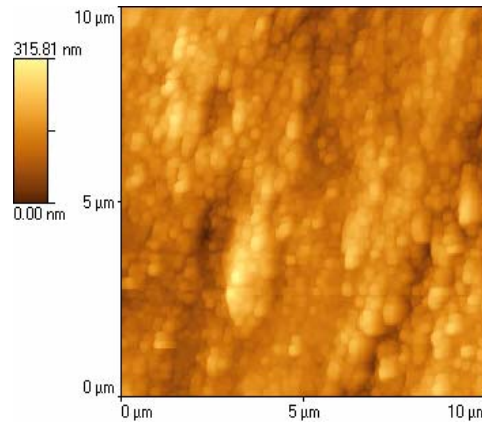


Fig. 6. Atomic force micrographs of compacted specimens obtained on 200 MPa.

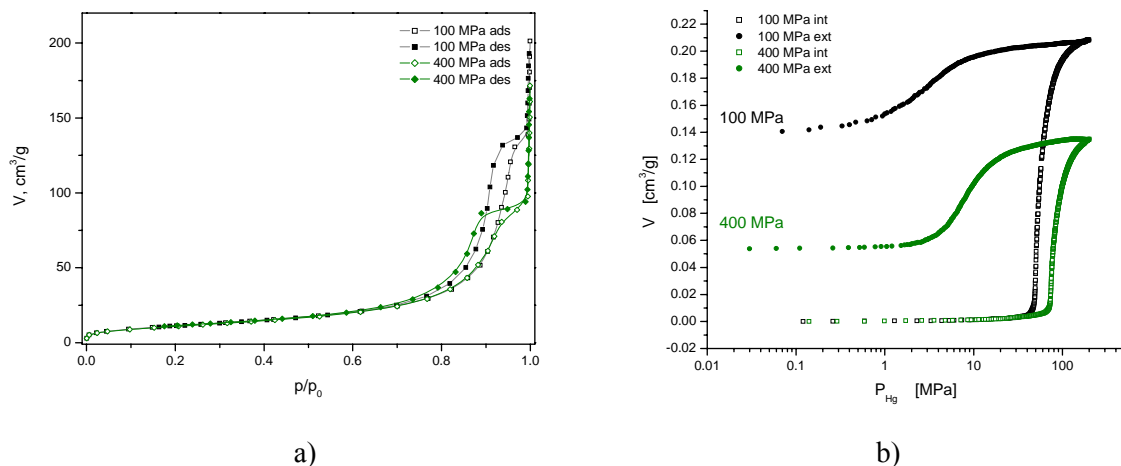


Fig. 7. a) Nitrogen adsorption-desorption isotherms and b) intrusion-extrusion mercury porosimetry curves for loose powder and compacts treated at 100 MPa and 400 MPa.

Compacted specimen’s adsorption-desorption nitrogen isotherms and mercury porosimetry intrusion–extrusion curves are presented on fig.7. a) and b) at the limits of the observed pressure intervals, 100 and 400 MPa. The two most obvious differences between the isotherms of compacts in Fig.7.a) and isotherm of loose powder in Fig.2.a), both especially pronounced for compacts at 400MPa, are: first – changes in the isotherm shape due to the existence of a plateau at higher relative pressures ($p/p_0 > 0.9$) and second - decrease of cumulative specific pore volume. Both isotherms of compacted specimens are type IV [18], which is characteristic for a material with a mesoporous structure. Hysteresis loops also change in shape from H1 for loose powder, to H2 for compacts [18]. This is due to the fact that the appearing form of particle-pore network in a loose powder samples differs from the one appearing in compacted samples. This difference originates from rounded agglomerates and a narrow pore size distribution (H1 type) in powder, to possible ink bottle shape of a pore network (H2 type) consisting of tubular pores surrounded with narrow constrictions in compacts. Large interagglomerate pores are of main interest for nanopowder sintering

process, and this hysteresis type difference strongly suggests that this type of pore – particle network is vanishing in the observed uniaxial compacting pressure domain.

Since the hysteresis loop ends above $0.42 p/p_0$, desorption branches were used for characteristic pore values calculations [22], tab.II. The steep part of the desorption branch indicates that ink bottle pores empty at once. This appearance correlating the relative pressure value p/p_0 of the steep part of the desorption branch with the critical radius constriction of the ink bottle shape pores. We can note that in observed pressure range the critical pore radius is lowered.

Nitrogen adsorption sets of data also reveal that monolayer completing is unaffected by the compaction process and further calculations of the specific surface area by two parameter BET procedure yields almost the same value for the specific surface area between compact specimens, tab.II., as well as when it is compared with the non compacted powder, fig.2.a). Here we can conclude that no powder particle fragmentation occurred during the compaction process.

Mercury porosimetry results for the same compaction pressures are presented in fig.7.b). We can say that inside the observed compaction pressure limits, all characteristic pore size values show the same behaviour trend, tab.II. Intrusion curves, unlike for the loose powder on fig.2.b), indicate that no mercury penetration occurs in the observed uniaxial compaction pressure range until the intrusion pressure near 40 MPa. An intensive sudden intrusion volume rise will give a relatively narrow pore size distribution. The pore structure accomplished with the compaction process also resembles ink bottle pore types, which can be deduced from the pronounced hysteresis. Relations between the intruded total cumulative pore volume and the extruded volume of mercury at the end of observed cycle, show that with the rise of applied compaction pressure, the amount of trapped mercury diminished.

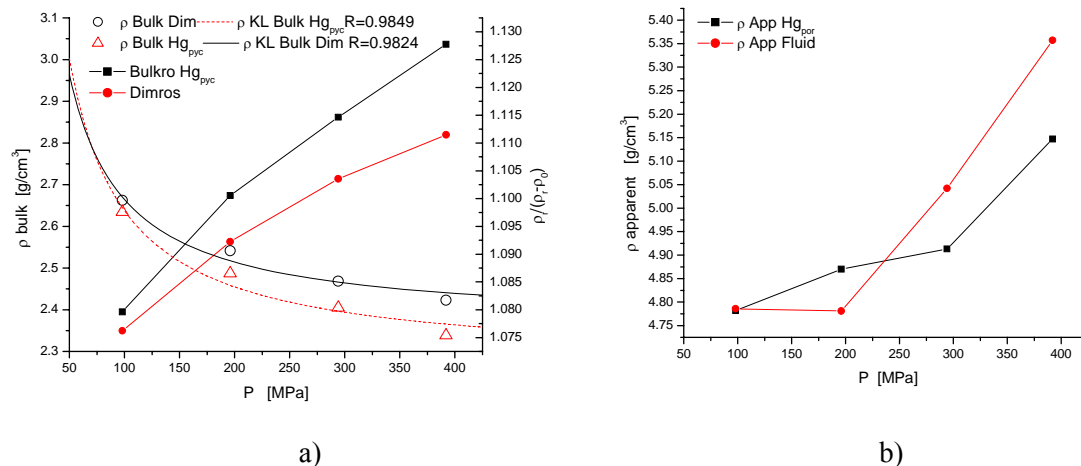


Fig. 8. a) Densities of green bodies as a bulk, obtained using dimension measurements and mercury pycnometry, in comparison with the relation to the curve formed by the Kawakita-Lüde compaction equation. **and b)** apparent density (of green body skeleton) obtained with mercury porosimetry and nitrogen adsorption.

Compaction is related to compact density as a function of the pressure scale. The density of a loose powder measured without taping on the same amount of powder weight as a compact's is termed ρ_0 and approximately is ten times the density value of the compact density at the lowest (100 MPa) pressure. Bulk densities refer to densities of compact shape volume including pore volume and are presented on fig. 8.a). They are obtained by mercury pycnometry and dimension measurements methods. Higher pycnometry values are due to the liquid mercury enclosure of all open pores volumes wider than $14 \mu\text{m}$ in diameter [22]. Lower

density values obtained by dimension measurements thus can be attributed to a presumed ideal cylindrical shape of compacts. Bulk densities can be fitted with the Kawakita-Lüde compaction equation [23] with R factor 0.9849 for mercury bulk and 0.9824 for dimension bulk densities. The Kawakita-Lüde compaction equation compacting equation is found to be the most convenient since it is mainly used for organic fluffy, materials compacted at low pressures showing high porosities [24]. Pore vanishing is followed as first order reaction on pressure in the used equation, viewed as a special case of the Heckel equation [25]. Organic materials show pore vanishing in narrow pressure domains, and ceramic nanopowders also lose their agglomerated ink bottle shaped pores in a narrow pressure range.

Apparent densities are defined here as the compacted specimens skeleton density. From the bulk volume determined with mercury pycnometry, pore volume is subtracted. Pore volume in our investigation was determined in two different ways. The first, denoted as ρ App Hg_{por}, is the intruded mercury volume during mercury porosimetry and the second is the pore volume obtained from the Gurvitch volume denoted as ρ App Fluid fig. 8.b). Since the fracture of nanoparticles due to pressure range and covalent atomic bonding is excluded [26], apparent density rise at higher pressures is subscribed to an increased powder particle's contact coordination number [20]. For mercury porosimetry the pore diameter calculated from the cumulative intruded volume reaches up to 7.5 nm and in nitrogen adsorption volume of fluid nitrogen uptake at 0.98 p/p₀, Gurvitsch volume, incorporates pore diameters calculated from the pore volume up to 2 nm. The micropore volume, tab.2, for pore diameters below 2 nm is also encountered in this calculation.

Apparent density at the lowest compaction pressure of 100 MPa shares the same value for both methods, since inter-agglomerate pores dominate in the overall pore volume. Differences between measuring techniques are significant after 200 MPa, where porosity between powder particles dominates inter-agglomerate pores and suitably ρ App Fluid density gives highest values.

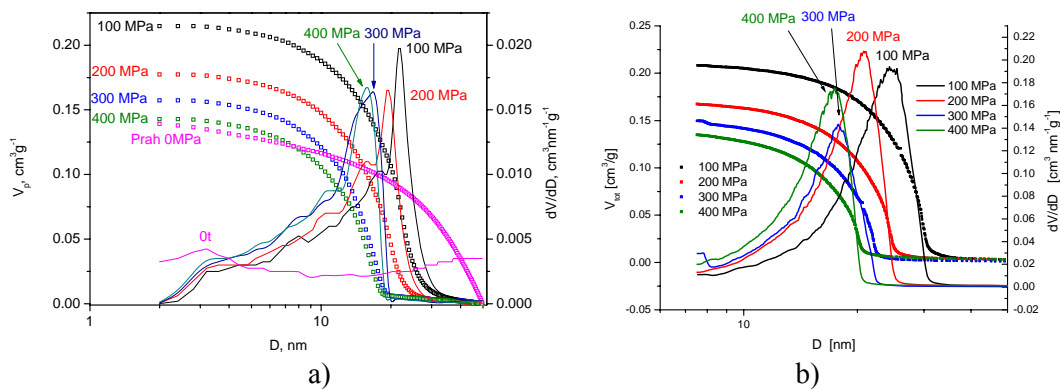


Fig. 9. Pore size distributions obtained with nitrogen adsorption **a)** and mercury porosimetry **b)** for compacts treated at 100, 200, 300 and 400 MPa.

Pore size distributions obtained from nitrogen adsorption and mercury porosimetry techniques, for compacts at all observed compaction pressures are presented on fig. 9.a) and b). Characteristic numerical values for porosity description of compacted samples are declared in tab.II

Tab. II Porosity measurements for compaction pressures 100 to 400 MPa

Measured pore property	Compaction pressure [MPa]				Pore characterization technique
	100	200	300	400	
Maximum pore diameter [nm]	24.5	20.8	17.8	17.4	Hg porosity
Maximum pore diameter [nm]	22.1	19.9	16.6	15.8	N ₂ desorption
Total cumulative pore volume [cm ³ /g]	0.208	0.167	0.146	0.133	Hg porosity
Cumulative pore volume [cm ³ /g]	0.218	0.179	0.165	0.149	N ₂ desorption
Gurvich p/p ₀ 0.98 pore volume [cm ³ /g]	0.208	0.168	0.151	0.137	N ₂ desorption
Micro pore volume, Dubinin [cm ³ /g]	0.014	0.014	0.014	0.014	N ₂ adsorption
Specific surface area [m ² /g]	42.1	40.0	41.1	40.8	N ₂ adsorption
Specific surface area [m ² /g]	35.4	34.3	33.9	32.8	Hg porosity

Nitrogen adsorption pore size is calculated with adsorbate-adsorbance correction [27]. For low pore diameters, determined group of microporous values at lowest partial nitrogen pressures by Dubinin-Radushkevich calculation [28], tab.II, neither indicates any kind of functional, nor even any trend, behaviour. Pore size distributions for both techniques are showing mutually very good resemblance in diameters of most populated pore size classes, fig.9.a) and b). Pore diameters for the most populated pores decrease until the compaction pressure reaches 200 MPa where they stop in the upper range of compaction pressures at approximately 17 nm. Since we noted an ink bottle shape type of pores it is also important to emphasize that lowering the pore size diameter value in the pore size distribution also indicates that inter-agglomerate pores are narrowing the critical radius of the constricted part of the pore. We can say that the inter-agglomerate pore network is vanishing in the lower observed uniaxial compacting pressure domain with two competitive processes: volumes of the reservoir part of the ink bottle shape pores in compacts are diminishing along with constriction critical radius lowering when the compaction pressure increases. Pore connectivity in the upper range of compaction pressures is hard to correlate with the particle coordination number, but the occurrence of laminar cracks at higher pressures than 400 MPa indicates that fine particles are not deformed by breakage and that the force distribution

instability is forming new interagglomerate cracks as the most convenient relaxing phenomenon. Presumably compacts after compaction die ejection along with residual elasticity lead to radial laminar crack propagation and suggest that the highest achievable powder particle coordination number is not reached.

4. Conclusion

Intensive agglomeration tendency for nanopowders is immanent to ZnTiO₃ nanopowder and uniaxially compacted specimens. Different nanopowder manipulation techniques influence inter-agglomerate and intra-agglomerate voids ratios, which is one of the main concerns regarding the consequent sintering process. Loose powder consisted of about 80 percent of inter-agglomerate cumulative pore volume. Agglomerates consisted of relatively weakly bonded nanopowder particles and the pressure limit for agglomerate crushing and mutual particles approach is estimated to be up to 30 MPa using mercury porosimetry. Uniaxially compacted specimens showed formation of inter-agglomerate pores with an ink bottle shape in the observed 100 - 400 MPa compaction pressure range. Densities of compacted specimens for bulk density followed the Kawakita-Lüde compacting equation, while the skeletal - apparent densities intensive raise can be attributed to nano-particle rearrangement processes. Pore size distribution of compacted specimens at compaction pressures higher than 200 MPa, reached a constant value of 17 nm for the most populated pore size class. This indicated that a further pressure increase above 400 MPa for this compaction experimental set up, would not lead to fine nanopowder particle deformation by breakage, but to an applied force distribution instability causing the formation of inter-agglomerate cracks.

5. References

1. V.M.Kenkre, M.R.Endicott, S.Jill Glass, A.J.Hurd, A Theoretical Model for Computation of Granular Materials, *J. Am. Ceram. Soc.* 79 [12] 3045-54 (1990).
2. I.Shapiro, Compaction of Powders XI, Application of the General Equation to Both Metal Powders and Ceramic Powders, *Adv. Powder Metall. Part. Mater.*, 3, 41-55 (1994).
3. N.Ozkan, B.J.Briscoe, Overall Shape of Sintered Alumina Compacts, *Ceramics International* 23 , (1997) 521-236.
4. P.Duwez, L.Zell, Pressure Distribution in Metal Powder Compacts, *Trans. AIME*, (1949), vol. 185, pp. 137-144.
5. R.M.German, Particle Packing Characteristics, Metal Powder Industries Federation, 1989.
6. М.Ю.Бальшин, Научные основы порошковой металлургии и металлургии волокна, М.:металлургия, 1972.
7. J.C.Kim, D.M.Martin, C.S.Lim, Effect of Rearrangement in Simulated Particle Packing, *Powder Technology*, 126, (2002), 211-216.
8. P.J.James, Fundamental Aspects of the Consolidation Process, *Powder metallurgy International*, Vol.4 no.4.(1972), *Powder metallurgy Review* 5.
9. B.J.Briscoe, N.Ozkan, Compaction of Agglomerated Alumina Powders, *Powder Technology* 90, (1997), 195-203.
10. A.C. Fischer-Cripps, The Herzian Contact Surface, *J.Mater.Sci.*, 34, (1999), pp. 129-137.

11. I.Krstanović, M.V.Nikolić, R.M.Novaković, Z.Nikolić, M.M.Živković, M.M.Risitić, A Mechanism for Cold Sintering of Copper Powder, Science of Sintering, 25(3), 145-153.(1993).
12. N.A.Fleck, G.M.Muller, M.F.Ashby, J.W.Hutchinson, Strain Gradient Plasticity: Theory and Experiment, Acta.Metall.Mater. Vol.42. No.2., pp.475-487, (1994)
13. Z.Wang, P.Lazor, S.K.Saxena, G.Artioli, High Pressure Raman Spectroscopic Study of Spinel ($ZnCr_2O_4$), Journal of Solid State Chemistry, 165, 165-170, (2002).
14. P.Bowen, C.Carry, From Powders to Sintered Pieces: Forming, Transformation and Sintering of Nanostructured Ceramic Oxides, Powder Technology, 128, (2002), 248-255.
15. M.Azar, P.Palmero, Effect of Initial Particle Packing on the Sintering of Nanostructure Alumina, Journal of European Ceramic Society, 28, (2008), 1121-1128.
16. Y.Kinemuchi, K.Watari, Dilatometer Analysis of Sintering Behaviour of Nano-CeO₂ Particles, Journal of European Ceramic Society, 28, (2008), 2019-2024.
17. International Centre for Diffraction Data, ZnTiO₃ 26-1500, Natl.Bur.Stand. (U.S.) Monogr., 25, 13, 49 (1976).
18. IUPAC, Reporting physisorption data for gas/solid systems, With special reference to the determination of surface area and porosity, (recommendations 1984), Pure and Applied Chemistry, Vol.57, No.4, pp.603-619, (1985).
19. C.Alie, R.Pirard, J.P.Pirard, Mercury porosimetry applicability of the buckling-intrusion mechanism to low density xerogels, Journal of Non-Crystalline Solids, 292, (2001), 138-149.
20. R.P.Mayer, R.A.Stowe, Mercury porosimetry: Filling of Toroidal Void Volume following Breakthrough between Packed Spheres, The Journal of Physical Chemistry, Vol.70, No.12, (1996), 3867-3873.
21. H.Giesche, Mercury Porosimetry: A General (Practical) Overview, Part.Part.Syst.Charact. 23, (2006), 1-11.
22. S.J.Gregg., K.S.W. Sing, Adsorption, Surface Area and Porosity, Academic Press Inc; 2nd Revised edition (April 1982).
23. K.Kawakita, K.-H. Lüdde, Some Considerations on Powder Compression Equations, Powder Technology, 4, [2], (1970-1971), 61-68.
24. P.J.Denny, Compaction equations: a comparison of the Heckel and Kawakita equations, Powder Technology, 127 (2002), 162-172.
25. R.W.Heckel, A Normalized Density Pressure Curve for Powder Compaction, Trans. Met. Soc., AIME 221 (1961) 671, 1001.
26. J.Binner, B.Vaidhyanathan, Processing of bulk nanostructured ceramics, Journal of the European Ceramic Society, 28, (2008), 1329-1339.
27. A.Lecloux, J.P.Pirard, The Importance of Standard Isotherms in the Analysis of Adsorption Isotherms for Determining the Porous Texture of Solids, Journal of Colloid and Interface Science, Vol.70., No.2., June 15, (1979), 265-281.
28. M.M.Dubinina, E.D.Zaverina, L.S. Ivanova, A Study of the Micropores Structure of Activated Charcoals, Russ.Chem.Bulletin, Vol.10, No.1, 129, (1961) 14-23, 24-30.

Садржај: $ZnTiO_3$ нанопрах представља материјал који се користи при процесу пресовања и карактерисан је непресован и нетретиран посебно. Снимљене су сканирајуће електронске микрографије праха. Методе живине порозиметрије и адсорпције азота такође су примењене на праху. Расподела величине честица праха у

воденој суспензији одређена је ласерским мерачем величине честица. Пресовање је рађено техником једноосног двостраног пресовања у опсегу притисака од 100 до 400 МПа без коришћења везива и подмазивача. Микрографије испресака добијене су сканирајућом електронском микроскопијом и микроскопијом међуатомске интеракције. Расподела величине пора одређена је живином порозиметријом као и адсорпцијом азота. Резултати су показали да се са повећањем притиска током пресовања поре између агрегата смањују док не досегну неки критични пречник који одговара величини пора унутар агрегата.

Кључне речи: Пресовање, нано прах, расподела величине пора, адсорпција азота, живина порозиметрија
